Check for updates

Pressure-driven structural phase transitions and metallization in the two-dimensional ferromagnetic semiconductor CrBr₃†

Meiling Hong,[a] Lidong Dai, 🆔 *[a] Haiying Hu,*[a] Xinyu Zhang,[a,b] Chuang Li[a,b] and Yu He[a,b]

High-pressure structural, magnetic and electrical transport characteristics of CrBr₃ were synthetically investigated using Raman scattering, electrical conductivity, high-resolution transmission electron microscopy (HRTEM) and first-principles theoretical calculations during compression and decompression under different hydrostatic conditions. Upon pressurization, CrBr₃ underwent a second-order structural transition at 9.5 GPa, followed by the semiconductor-to-metal and magnetic switching at 25.9 GPa under non-hydrostatic conditions, whereas, an obvious pressure hysteresis of ~3.0 GPa was detected in the occurrence of structural transitions and metallization under hydrostatic conditions due to the deviatoric stress. Upon decompression, the structural and electronic transitions of CrBr₃ under different hydrostatic conditions were of good reversibility with a considerable pressure sluggishness of ~5.0 GPa, which was corroborated well by the microstructural observation with HRTEM. Our systematic high-pressure investigation on CrBr₃ not only reveals its underlying application in spintronic, magnetic and electronic devices but also advances the understanding of the physicochemical behaviors for 2D magnetic materials.

Introduction

Two-dimensional (2D) chromium trihalide CrX₃ (X = Cl, Br and I) compounds, emergent magnetic semiconductors, have attracted tremendous interest in terms of both fundamental research and technological application owing to their exceptional optical, electronic and magnetic properties.[1,2] CrX₃ belong to the class of layered van der Waals materials where each chromium atom is surrounded by six halide atoms in a hexagonal honeycomb network and the formed X–Cr–X tri-layers are stacked along the vertical c axis direction by weak van der Waals forces.[2–4] Compared with other CrX₃ compounds, chromium tribromide (CrBr₃) has some exotic properties, *e.g.*, the structural stability at low temperature and the similarity in magnetic ordering for bulk and monolayers.[5–7] Under ambient conditions, CrBr₃ is a ferromagnetic semiconductor with a Curie temperature of 47 K and a wide bandgap energy of 1.38 eV, which crystallizes into a rhombohedral structure with the symmetry of $R\bar{3}$.[8] In light of the extra-

ordinary physicochemical behaviours, CrBr₃ is a promising material in optical isolators, magnetic sensors and rewritable optical memory.[9]

The application of pressure offers an effective approach of manipulating the structural, magnetic and electrical transport characteristics of chromium trihalides.[10–13] Despite the considerable high-pressure investigations on CrCl₃ and CrI₃, only one unique available research on CrBr₃ under high pressure has been reported to date.[10–13] More recently, CrCl₃ has been revealed to endure an isostructural phase transition (IPT) at 9.9 GPa, which was concurrent with the magnetic crossover from ferromagnetic (FM) to antiferromagnetic (AFM) configurations.[10,11] On further compression up to 28.0 GPa, an electronic topological transition (ETT) occurred, accompanying the emergence of semiconductor-to-metal transformation in CrCl₃.[10,11] For chromium triiodide, the pressure-driven metallization and magnetic transformation took place simultaneously as the pressure increased above 22.0 GPa, which was corroborated by the theoretical calculation results with the overlap of valence bands and conduction bands,[12] whereas, for chromium tribromide, the high-pressure structural, magnetic and vibrational behaviours were studied through X-ray powder diffraction, neutron powder diffraction and Raman spectroscopy up to a limited pressure of 23.0 GPa.[13] Their results demonstrated that CrBr₃ experienced a pressure-induced IPT within the pressure range of 2.5–7.0 GPa. As the pressure

[a] *Key Laboratory of High-Temperature and High-Pressure Study of the Earth's Interior, Institute of Geochemistry, Chinese Academy of Sciences, Guiyang, Guizhou 550081, China. E-mail: dailidong@vip.gyig.ac.cn, huhaiying@vip.gyig.ac.cn*
[b] *University of Chinese Academy of Sciences, Beijing 100049, China*
† Electronic supplementary information (ESI) available. See DOI: https://doi.org/10.1039/d3dt00899a

increased to ~15.0 GPa, another structural transition occurred in $CrBr_3$, which was possibly associated with the proximity of metallization.[13] However, no robust evidence is provided to verify the presence of electronic transitions in $CrBr_3$ under high pressure and its phase stability beyond 23.0 GPa remains unclear.

On the other hand, the deviatoric stress has been considered as a critical ingredient affecting the high-pressure phase stability, structural transition pressure and the reversibility of phase transformation for 2D layered semiconducting materials.[11,14–21] Hong *et al.* (2022) have studied the high-pressure Raman spectra of $CrCl_3$ under different hydrostatic conditions and a ~2.0 GPa pressure delay in the emergence of IPT and metallization was detected under hydrostatic conditions owing to the relatively feeble deviatoric stress.[11] However, to date, there is no related report on the influence of deviatoric stress on the high-pressure structural behaviour of $CrBr_3$ under different hydrostatic conditions.

In the present work, the high-pressure structural, magnetic and electrical transport characterization of $CrBr_3$ was comprehensively performed under different hydrostatic conditions using a diamond anvil cell up to 41.3 GPa by virtue of *in situ* Raman spectroscopy, alternating current (AC) impedance spectroscopy, HRTEM and first-principles theoretical calculations. Furthermore, the pressure-induced structural transition, metallization and magnetic crossover of $CrBr_3$ upon compression and decompression processes were sufficiently discussed.

Results and discussion

High-pressure Raman spectra of $CrBr_3$

Fig. 1a–c display the high-pressure Raman spectra of $CrBr_3$ with a rise of pressure up to 37.6 GPa under non-hydrostatic conditions. The corresponding evolution of Raman shifts as a function of pressure is plotted in Fig. 1d. It makes clear that four characteristic Raman peaks at the positions of 105.8 cm^{-1} (A_g), 136.5 cm^{-1} (E_g), 148.3 cm^{-1} (E_g) and 182.7 cm^{-1} (A_g) are observed at a fixed pressure of 0.9 GPa within the wavenumber range of 100–400 cm^{-1}. Overall, our acquired Raman peaks are in excellent agreement with previous studies.[5,13,22–24] To draw a clear distinction between different Raman modes of $CrBr_3$, we defined the Raman peaks at 105.8, 136.5, 148.3 and 182.7 cm^{-1} as the A_g^1, E_g^1, E_g^2 and A_g^2 modes of $CrBr_3$, respectively.

It can be seen clearly from Fig. 1a–c that all the Raman peaks of $CrBr_3$ monotonically shifted towards higher wavenumbers with increasing pressure. Noteworthily, the spacing between A_g^1 and E_g^1 Raman peaks diminished considerably with the application of pressure owing to the evident discrepancy in their slopes of Raman shifts. On further compression to 9.5 GPa, the A_g^1 and E_g^1 Raman peaks merged into a single peak. Actually, a similar mergence phenomenon of A_{g2} and A_{g3} Raman scattering peaks in $CrCl_3$ was also observed at 9.9 GPa, which resulted from the occurrence of pressure-induced IPT.[11]
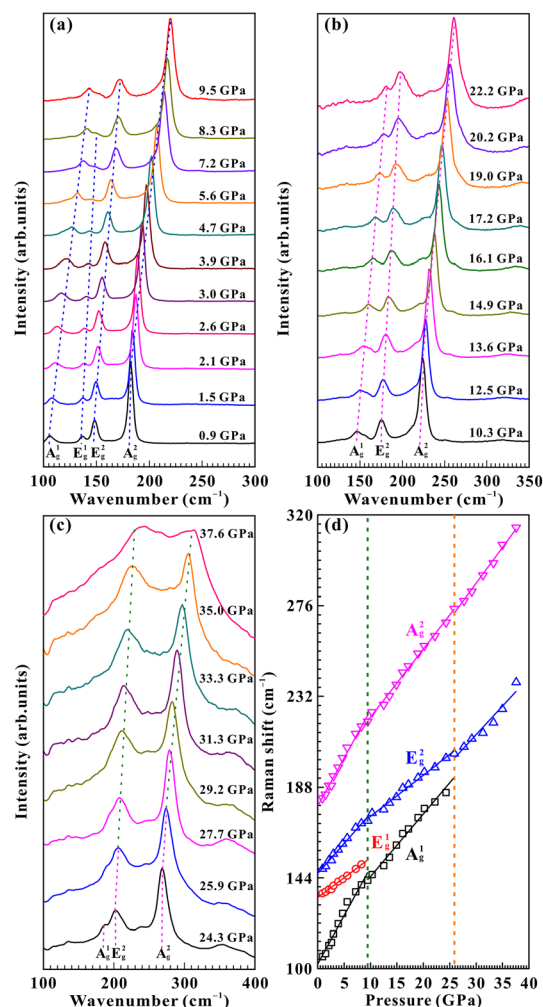

Fig. 1 (a)–(c) High-pressure Raman spectroscopy results of $CrBr_3$ within the pressure range of 0.9–37.6 GPa upon compression at room temperature. (d) The evolution of Raman shifts as a function of pressure for $CrBr_3$ under non-hydrostatic conditions.

Beyond 9.5 GPa, the A_g^1 characteristic Raman peak of $CrBr_3$ tended to weaken progressively with the rise of pressure and vanished completely at 25.9 GPa. Afterwards, as the pressure exceeded 25.9 GPa, the remaining Raman peaks of the sample exhibited substantial broadening and remarkable weakening up to the highest experimental pressure of 37.6 GPa.

Table S1† summarizes the pressure coefficient ($d\omega/dP$) of $CrBr_3$ calculated from the linear fitting equation of $\omega(P) = \omega(P_0) + (d\omega/dP)P$ during both processes of compression and decompression under different hydrostatic conditions, which plays a crucial role in signifying the emergence of the pressure-driven structural transition of CrX_3 compounds.[10–13] Simultaneously, the pressure dependence of Raman full width at half maximum (FWHM) and spacings in Raman shifts are illustrated in Fig. 2 and 3, and further, their corresponding fitting results upon compression and decompression under different hydrostatic conditions are listed in Tables S2 and S3,† respectively. More importantly, the pressure coefficients
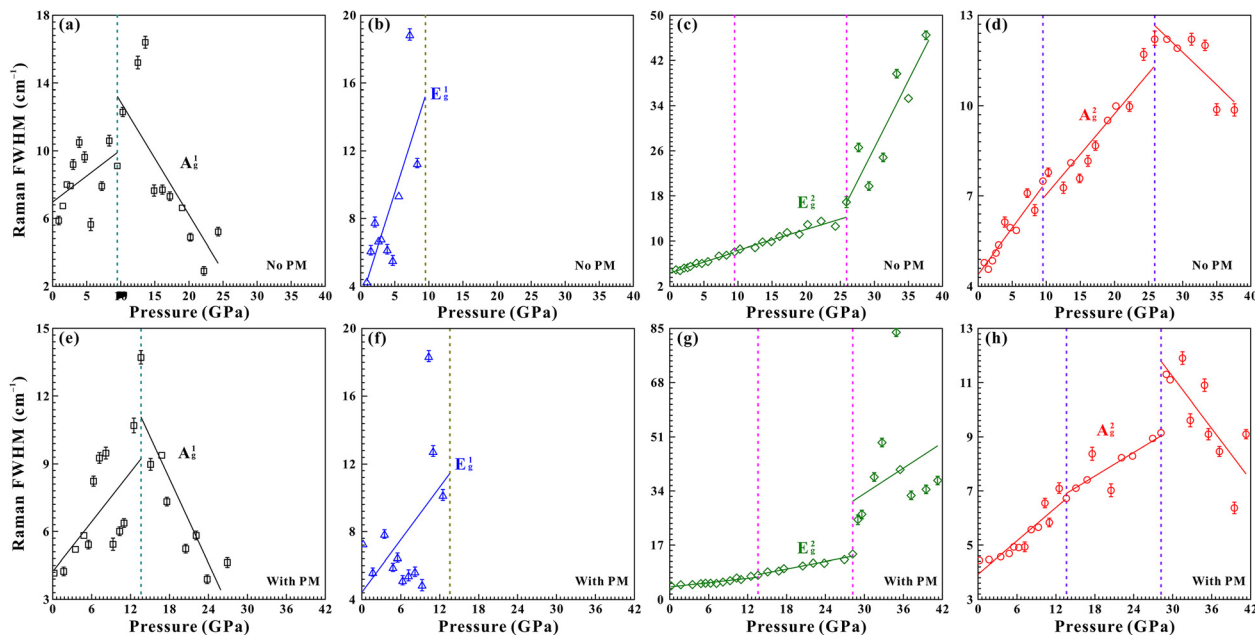
Fig. 2 Raman FWHM results of CrBr$_3$ with increasing pressure for (a) A$_g^1$, (b) E$_g^1$, (c) E$_g^2$ and (d) A$_g^2$ modes under non-hydrostatic conditions and (e) A$_g^1$, (f) E$_g^1$, (g) E$_g^2$ and (h) A$_g^2$ modes under hydrostatic conditions. Here, PM denotes the pressure medium.
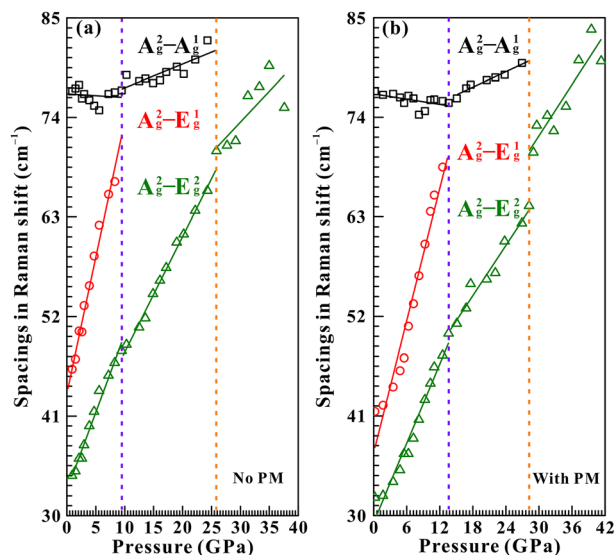

Fig. 3 The spacings in Raman shifts against pressure for CrBr$_3$ under (a) non-hydrostatic conditions and (b) hydrostatic conditions, respectively. Herein, PM stands for the pressure medium.

of A$_g^1$ and A$_g^2$ modes converted from the steeper values of 4.66 and 4.62 cm^{-1} GPa^{-1} at the correspondent pressure lower than 9.5 GPa to moderate values of 3.04 and 3.31 cm^{-1} GPa^{-1} within the subsequent pressure range of 9.5–25.9 GPa, respectively. Meanwhile, the FWHM of A$_g^1$ mode showed an evident discontinuity at 9.5 GPa. Regarding the spacings in the Raman shift for A$_g^2$–A$_g^1$, its slope changed from −0.042 cm^{-1} GPa^{-1}

below 9.5 GPa to 0.26 cm^{-1} GPa^{-1} at 9.5–25.9 GPa. Furthermore, the FWHM of E$_g^2$ mode increased marginally at a rate of 0.36 cm^{-1} GPa^{-1} within the pressure range of 9.5–25.9 GPa, whereas it possessed a larger rate of 2.38 cm^{-1} GPa^{-1} at 25.9–37.6 GPa. As for the FWHM of A$_g^2$ mode, its slope experienced a distinct sign reversal from positive to negative at 25.9 GPa. Taken together, upon pressurization, the mergence of A$_g^1$ and E$_g^1$ modes, the noticeable discontinuities in the pressure dependence of Raman shifts for A$_g^1$ and A$_g^2$ modes, the FWHM for A$_g^1$ mode and spacings in the Raman shift for A$_g^2$–A$_g^1$ provided solid evidence for the occurrence of a phase transition in CrBr$_3$ at 9.5 GPa. When the pressure increased to 25.9 GPa, the disappearance of A$_g^1$ mode and the prominent inflection points in the FWHMs of E$_g^2$ and A$_g^2$ modes were indicative of another structural transition in CrBr$_3$.

Fig. 4a–c illustrate the high-pressure Raman spectra of CrBr$_3$ during decompression and the relevant relationship of Raman shifts *versus* pressure is plotted in Fig. 4d. It makes clear that the E$_g^2$ and A$_g^2$ Raman peaks of the sample presented red shifts, accompanied by the progressive enhancement in their Raman peak intensities with decreasing pressure. Notably, the A$_g^1$ Raman peak at 181.4 cm^{-1} reappeared as the pressure relieved to 21.7 GPa. Additionally, the pressure coefficient of A$_g^2$ mode exhibited a discernable inflection point at 21.7 GPa. On further decompression to 5.0 GPa, another Raman peak centered at 151.0 cm^{-1} reemerged, which corresponded to the E$_g^1$ mode of CrBr$_3$. Concomitantly, both the pressure coefficients of A$_g^1$, E$_g^2$ and A$_g^2$ modes, and the spacings in Raman shifts for A$_g^2$–A$_g^1$ and A$_g^2$–E$_g^2$ modes showed pronounced discontinuities at 5.0 GPa. Consequently, our Raman scattering results on CrBr$_3$ during decompression
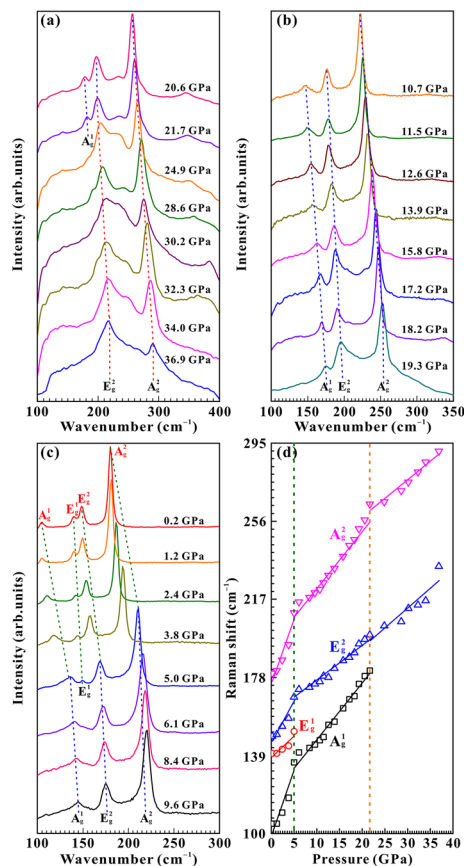
Fig. 4 (a)–(c) High-pressure Raman spectra of $CrBr_3$ within the pressure range of 36.9–0.2 GPa and room temperature during decompression. (d) Corresponding variation of Raman shifts as a function of pressure under non-hydrostatic conditions.

numerous materials, thereby giving rise to the emergence of structural and electronic transitions. The anisotropic stress was inevitable under both non-hydrostatic and hydrostatic conditions. More importantly, the magnitude of anisotropic stress highly depends on the hydrostaticity within the sample chamber of the diamond anvil cell.[25] As the pressure increases, the anisotropic stresses and non-uniform deformations are larger under non-hydrostatic conditions compared to those under hydrostatic conditions, which plays a vital role in promoting the occurrence of structural and electronic transitions in the extensive materials family of two-dimensional chromium trihalides and other non-layered materials.[11,26–29] Consequently, the observed higher structural and electronic transition pressures of $CrBr_3$ under hydrostatic conditions relative to those under non-hydrostatic conditions can be well explained by the smaller anisotropic stresses.

Both Lis *et al.* (2023) and us explored the high-pressure phase stability of $CrBr_3$ and identified the occurrence of two structural transitions in $CrBr_3$ during the process of compression by means of Raman spectroscopy.[13] Furthermore, we found that the electronic transitions identified by Lis *et al.* (2023) resemble the first structural transition in our work.[13] However, compared with our obtained transition pressures of 9.5 and 25.9 GPa, lower transition pressures of 2.5–7.0 GPa and ~15.0 GPa were reported by Lis *et al.* (2023). To be specific, they determined the first structural transition of $CrBr_3$ at 2.5–7.0 GPa by the pronounced discontinuities in the lattice constant (c) and volume, and the appearance of the M1 Raman peak along with the obvious inflection point in the pressure coefficient of A_g^1 mode. At ~15.0 GPa, the mergence of E_g^2 and M1 Raman peaks together with the discontinuity in the pressure coefficient of A_g^1 mode were indicative of the occurrence of metallization in $CrBr_3$. In our present study, the M1 Raman peak has not been observed up to the highest experimental pressure of 37.6 GPa, which is possibly related to the broad A_g^1 Raman peak. Nevertheless, the disappearance of the A_g^1 Raman peak due to the limited experimental pressure of 23.0 GPa has not been detected. The above-mentioned discrepancies between Lis *et al.* (2023) and us is probably ascribed to (i) the starting sample and (ii) the laser wavelength and power of the applied Raman spectrometer.

High-pressure electrical conductivity

Fig. 5a–c show the typical complex impedance spectra of $CrBr_3$ within the pressure range of 1.7–40.5 GPa and atmospheric temperature. Below 24.6 GPa, the impedance spectra of the sample display approximate semicircular arcs with their centers on or slightly below the real part (Z') of complex impedance in the high-frequency region plus the inclined lines in the low-frequency region, which corresponds to the grain interior and grain boundary contributions of the $CrBr_3$ sample, respectively. To quantitatively extract the electrical resistances of $CrBr_3$ under pressure, an equivalent circuit composed of a parallel resistor (R) and a constant phase element (CPE) is applied to fit high-frequency semicircles using Zview software. As the pressure approached 24.6 GPa, a line perpen-

demonstrated the reversal of two high-pressure structural transitions at the respective pressures of 21.7 and 5.0 GPa, albeit with the existence of a pressure sluggishness of ~5.0 GPa.

Fig. S1 and S2† depict the high-pressure Raman spectroscopic results of $CrBr_3$ and the related pressure dependent Raman shift relationships upon compression and decompression processes under hydrostatic conditions. Noteworthily, both the high-pressure Raman spectra of $CrBr_3$ and the corresponding evolution of Raman shifts, FWHMs and spacings in Raman shifts with applied pressure under hydrostatic conditions followed a similar trend to that under non-hydrostatic conditions. As shown in Fig. 2, 3 and S1,† $CrBr_3$ underwent two structural transformations at higher pressures of 13.6 and 28.2 GPa under hydrostatic conditions compared to those of 9.5 and 25.9 GPa under non-hydrostatic conditions. From Fig. S2 and S3,† the reversal of phase transitions occurred at 24.8 and 6.9 GPa upon decompression. As seen in Fig. 4c and S2c,† the recovery of the Raman spectrum further confirmed the reversibility of the structural transitions under different hydrostatic conditions. It is well known that strain is an effective and crucial parameter regulating the interatomic interaction, electronic orbital and crystalline structure of
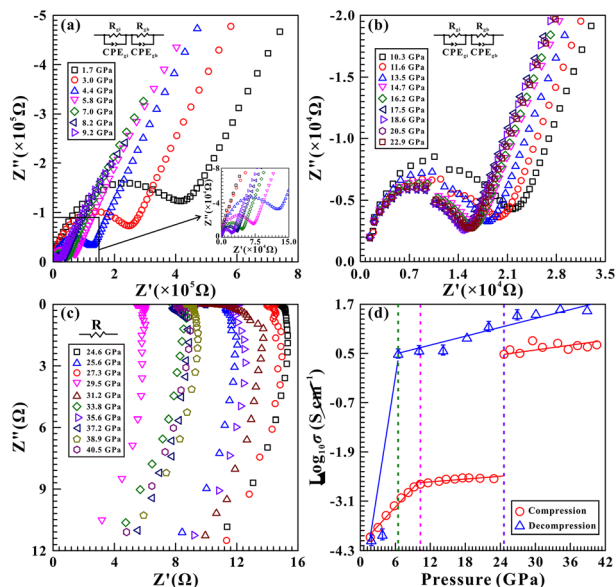
Fig. 5 Nyquist plots of impedance spectroscopy for CrBr$_3$ within the pressure ranges of (a) 1.7–9.2 GPa; (b) 10.3–22.9 GPa and (c) 24.6–40.5 GPa at atmospheric temperature under compression. Herein, R_{gi} and R_{gb} represent the resistances of grain interior and grain boundary for the CrBr$_3$ sample, respectively. CPE$_{gi}$ and CPE$_{gb}$ are the constant phase elements of the grain interior and grain boundary for the CrBr$_3$ sample, respectively. Z' and Z'' stand for the real and imaginary parts of complex impedance. (d) Pressure dependence of electrical conductivity for CrBr$_3$ under both compression and decompression processes.

dicular to the real part (Z') of complex impedance emerged, which is modeled by a resistor (R). Subsequently, the electrical conductivity (σ) of CrBr$_3$ was calculated from the resistance (R) and the geometric factor L/S (where S and L represent the cross-section area of the electrode and the distance between the electrodes) based on the equation $\sigma = L/SR$. The corresponding logarithmic electrical conductivity of CrBr$_3$ against pressure is illustrated in Fig. 5d. Noticeably, three regions were distinguished from the pressure dependence of the electrical conductivity relationship of CrBr$_3$. Below 10.3 GPa, the electrical conductivity of CrBr$_3$ substantially increased with increasing pressure at a steep slope of 0.15 S cm^{-1} GPa^{-1}. However, a feeble enhancement in the electrical conductivity of the sample was detectable between 11.6 and 22.9 GPa. The remarkable discontinuity in electrical conductivity at 10.3 GPa matches well with the high-pressure Raman scattering results under non-hydrostatic conditions and is probably associated with the first structural transition of CrBr$_3$. Noteworthily, the electrical conductivity of the sample reached up to 0.48 S cm^{-1} at 24.6 GPa, which is comparable to the electrical conductivity of a metal material.[11,14–16,18–20] Above 24.6 GPa, the electrical conductivity of CrBr$_3$ was weakly dependent on pressure at a gentle slope of 0.0092 S cm^{-1} GPa^{-1}. Upon decompression, the electrical conductivity of the sample diminished as the pressure was released. Furthermore, an available critical pressure of 6.4 GPa was observed in the pressure dependent electrical conductivity relationship, which is correlated with

the phase transformation of CrBr$_3$. Additionally, the recoverable electrical conductivity magnitude of CrBr$_3$ at 1.9 GPa further confirmed the reversibility of structural transitions.

To corroborate the occurrence of metallization in pressurized CrBr$_3$, the variable-temperature electrical conductivity measurements during the compression and decompression processes as well as their corresponding temperature-pressure-electrical conductivity contour maps are displayed in Fig. 6, 7 and Fig. S4.† Generally speaking, the electrical conductivity of a semiconductor increases profoundly with the rise of temperature ($d\sigma/dT > 0$), whereas a metal has a faintly negative temperature dependence in the electrical conductivity relationship ($d\sigma/dT < 0$).[11,12,15–20,30–32] As seen in Fig. 6a and b, during compression, CrBr$_3$ exhibited a positive $d\sigma/dT$ relationship below 23.8 GPa, which is characteristic of the semiconducting behaviour. Above 25.2 GPa, the negative $d\sigma/dT$ relationship implied the metallization of CrBr$_3$. Besides, this makes it clear that the electrical conductivity of CrBr$_3$ displays a large tunable range across almost seven orders of magnitude with the occurrence of the transformation from semiconductor to metal phases (see Fig. 7). Furthermore, above 25.9 GPa, a substantial reduction in the intensity of the Raman peak is probably related to the metallic feature of the CrBr$_3$ sample. From Fig. S4a and b,† upon decompression, the negative $d\sigma/dT$ relationship above 8.1 GPa represented the metallic properties of the sample. Below 5.7 GPa, the semiconducting behaviour of CrBr$_3$ was disclosed from the positive $d\sigma/dT$ relationship. In sum, our electrical conductivity results revealed that CrBr$_3$
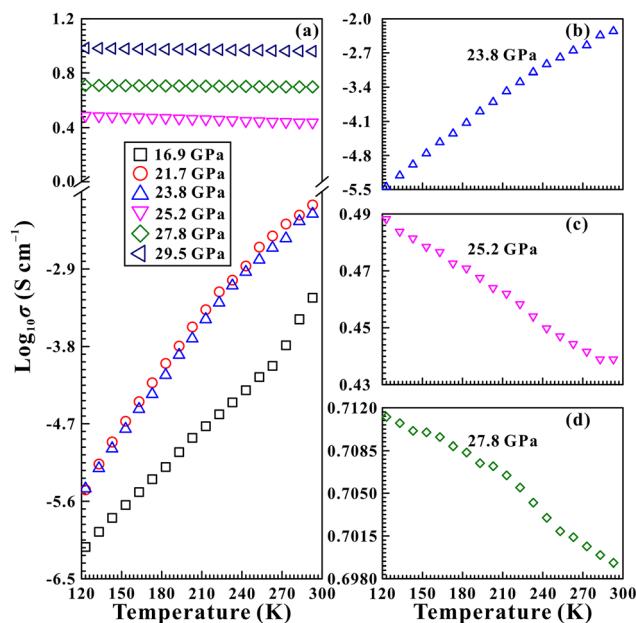

Fig. 6 A series of variable-temperature electrical conductivity measurements on CrBr$_3$ at several representative pressures. Herein, (a) denotes all results at 16.9, 21.7, 23.8, 25.2, 27.8 and 29.5 GPa upon compression; (b) denotes the typical semiconducting behaviour of CrBr$_3$ at 23.8 GPa; (c) denotes the metallic properties at 25.2 GPa and (d) denotes the metallic state of the sample at 27.8 GPa, respectively.
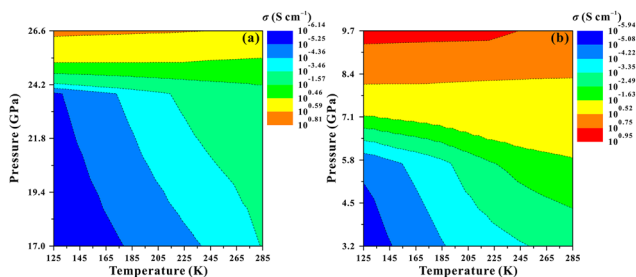
Fig. 7 Temperature–pressure–electrical conductivity contour maps for $CrBr_3$ during the compression (a) and decompression (b) processes, respectively.

underwent a phase transition at 10.3 GPa followed by the appearance of metallization at 24.6 GPa upon pressurization. During decompression, the electronic transition of the sample showed good reversibility with a considerable pressure hysteresis of ~18.0 GPa, which is possibly caused by the intrinsic crystal structure of chromium trihalides.[11] As for the inconsistent results on the phase stability of $CrBr_3$ at ~22.0 GPa during decompression obtained from Raman spectroscopy and electrical conductivity measurements, the different sensitivity between the two measurement methods is the most possible cause.

In consideration of the similarities in the crystalline and electronic band structures of CrX_3 (X = Cl, Br and I) compounds under ambient conditions, it is reasonable to extrapolate that the analogous structural and electrical transport properties are possible under high pressure.[33] Hence, a detailed comparison was conducted on the evolution of electrical conductivity as a function of pressure for CrX_3 (X = Cl, Br and I) compounds at atmospheric temperature, as presented in Fig. S5.† It is evident that the pressure dependent electrical conductivity relationship in $CrCl_3$ resembles that in $CrBr_3$ with a noticeable inflexion point in electrical conductivity at structural transition pressure followed by a sudden jump in electrical conductivity at around metallization pressure. In contrast to $CrCl_3$ and $CrBr_3$, the absence of structural transition in CrI_3 up to ~40.0 GPa is presumably related to the more delocalized 5p orbitals of the iodine atom than the 3p and 4p orbitals of chlorine and bromine atoms, which leads to better hybridization of chromium 3d and iodine 5p orbitals and thus stronger interlayer interactions.[34–36] Besides, unlike the abrupt enhancement in the electrical conductivity of $CrCl_3$ and $CrBr_3$ at around metallization, the progressive increase of electrical conductivity in CrI_3 indicated the continuous tunability of its electronic structure and bandgap energy under high pressure. Furthermore, more detailed comparisons of the pressures of structural and electronic transitions for CrX_3 compounds upon compression and decompression under different hydrostatic conditions are listed in Table S5.† As a whole, it is clear that the structural transition and metallization pressures of CrX_3 compounds evolved regularly as the atomic radius of the halogen increased from chlorine, bromine to iodine. In particular, with increasing atomic radius, the pressures of struc-

tural and electronic transitions decreased gradually in order from $CrCl_3$, $CrBr_3$ to CrI_3, which satisfies the pressure homology principle.[37,38] The middle transition pressures for $CrBr_3$ are probably associated with the appropriate atomic radius and electron orbitals of bromine in comparison with those of chlorine and iodine, leading to a moderate electronic coupling effect. As a matter of fact, a similar high-pressure behaviour has been disclosed in the recently reported other representative 2D layered transition-metal disulfides, such as MoX_2 (X = S, Se and Te) and HfX_2 (X = S, Se and Te).[20,34] In summary, this is the first time that the structural and electronic phase transformations of $CrBr_3$ are thoroughly revealed at higher pressures up to 41.3 GPa, and in comparison with the existence of the helium pressure medium under hydrostatic conditions, we found pressure sluggishness values of 4.1 and 2.3 GPa during compression together with 1.9 and 3.1 GPa upon decompression, respectively.

HRTEM of $CrBr_3$

Fig. 8 shows the representative cross-section HRTEM images and the corresponding fast Fourier transform (FFT) patterns for the initial and recovered samples under different hydrostatic conditions. As seen in Fig. 8a, the vivid and homogeneous lattice stripes in the HRTEM image suggest the well-crystallized initial sample. Subsequently, the interplanar spacing of the starting sample was found to be ~0.42 nm, and can be identified as the (103) crystallographic plane of rhombohedral $CrBr_3$. The corresponding FFT pattern of the HRTEM image exhibited well-defined bright diffraction spots immersing in a dark background, which further revealed a single crystalline initial sample with high crystal quality. As illustrated in Fig. 8a–f, the analogous interplanar spacing values and FFT patterns for the pristine and retrieved samples validated the reversibility of structural transitions under different hydrostatic conditions. Compared with the FFT pattern of the
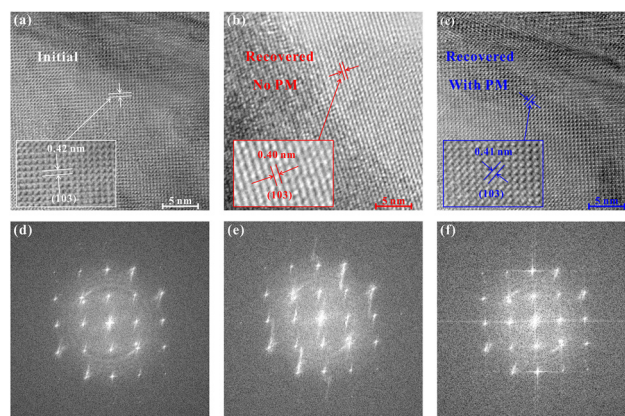

Fig. 8 Bright-field HRTEM images and their correspondent FFT patterns for $CrBr_3$. The scale bar is 5 nm. (a) and (d) The images of the initial sample. (b) and (e) The images for the recovered sample decompressed from 36.8 GPa under non-hydrostatic conditions. (c) and (f) The images for the retrieved sample decompressed from 40.3 GPa under hydrostatic conditions. Therein, PM represents the pressure medium.

decompressed sample under hydrostatic conditions, the slightly fuzzy diffraction spots in the FFT pattern for the recovered sample under non-hydrostatic conditions are possibly associated with the absence of pressure medium. As we know, the presence of pressure medium plays a significant role in alleviating the interlayer interaction and thus leads to the well-preserved crystalline structure of the decompressed sample under hydrostatic conditions, as previously reported in other 2D layered semiconducting materials.[11,14–20]

First-principles theoretical calculations of CrBr$_3$

To unravel the underlying mechanism of the high-pressure magnetic and structural transitions in CrBr$_3$, the first-principles theoretical calculations were carried out within the pressure range of 1–40 GPa at the Hefei Advanced Computing Center of China. The enthalpies of different magnetic ordering of CrBr$_3$ including the FM, AFM and M12 phases were calculated at 10–35 GPa under conditions of two representative U values (U = 2.0 eV and U = 3.2 eV). Herein, the enthalpy of the ferromagnetic CrBr$_3$ was set as the reference. As illustrated in detail in Fig. 9a, at a fixed U value of 2.0 eV, the enthalpy of the FM phase of CrBr$_3$ intersected with that of the M12 phase at ~17 GPa, whereas the enthalpy of the AFM phase was always higher than that of the M12 phase in our calculated pressure range of 10–35 GPa. Therefore, the FM phase of CrBr$_3$ will transform into the M12 phase at ~17 GPa. However, for the corresponding U value of 3.2 eV, the FM-to-M12 magnetic phase transition occurred at a higher pressure of ~23 GPa. Thus, this makes it clear that the magnetic transition pressure of CrBr$_3$ is highly sensitive to the magnitude of the Hubbard U value, which has also been reported in previous theoretical calculation results for the isostructural chromium trihalides of CrCl$_3$ under high pressure.[10] Furthermore, the electronic band structures, density of states, and crystallographic parameters of different magnetic CrBr$_3$ were calculated at a fixed U value of 2.0 eV. Fig. 10 shows the electronic band structures and the corresponding density of states for the FM phase of CrBr$_3$ at 25 GPa, the M12 phase of CrBr$_3$ at 25 GPa and the AFM phase

Fig. 10 (a) and (b) represent the calculated electronic band structures and density of states for the FM phase of CrBr$_3$ at 25 GPa. (c) and (d) represent the calculated electronic band structures and density of states for the M12 phase of CrBr$_3$ at 25 GPa. (e) and (f) represent the calculated electronic band structures and density of states for the AFM phase of CrBr$_3$ at 30 GPa. (a, c and e) Calculated electronic band structures and (b, d and f) their corresponding density of states for FM, M12 and AFM configurations of CrBr$_3$ at the respective pressures of 25, 25 and 30 GPa. Herein, FM and AFM stand for the ferromagnetic and antiferromagnetic orders of CrBr$_3$, respectively.

of CrBr$_3$ at 30 GPa. Clearly, the bandgap energy of the FM phase of CrBr$_3$ at 25 GPa is ~0.82 eV and a smaller bandgap energy of ~0.58 eV was obtained for the AFM phase of CrBr$_3$ at 30 GPa. Noteworthily, as seen from Fig. 10c, the bandgap closed for the M12 phase of CrBr$_3$ at 25 GPa, indicating the metallic behavior. Therefore, the magnetic transition of CrBr$_3$ is possibly accompanied by the occurrence of metallization, which has also been reported in the chromium triiodide with a similar crystalline structure of 2D chromium trihalide.[12]

Several crucial crystallographic parameters of the sample, including the lattice constants (a, b and c), normalized lattice constants (a/a_0, b/b_0 and c/c_0), lattice constant ratios (a/c and b/c), unit cell volume (V), normalized unit cell volume (V/V_0), Cr–Br–Cr bond angle, Cr–Br bond length, nearest Cr–Cr bond length and 2nd nearest Cr–Cr bond length, as a function of pressure were successfully obtained, and a series of representative results are displayed in Fig. 11 and Fig. S6.† As illustrated
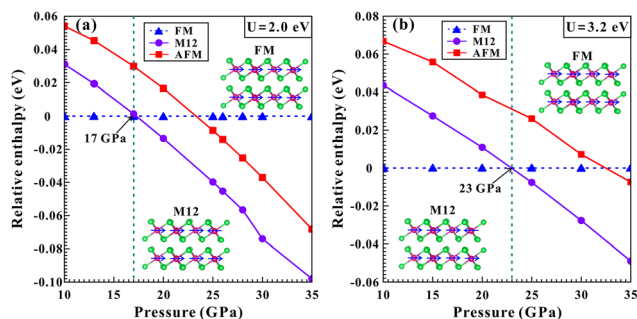

Fig. 9 Theoretical calculation results of the enthalpies of different magnetic orderings of CrBr$_3$ within the pressure range of 10−35 GPa under two typical Hubbard U values of (a) 2.0 eV and (b) 3.2 eV, respectively. The enthalpy of the ferromagnetic CrBr$_3$ was set as the reference. Inset: schematic crystal structures of the FM and M12 configurations of CrBr$_3$.
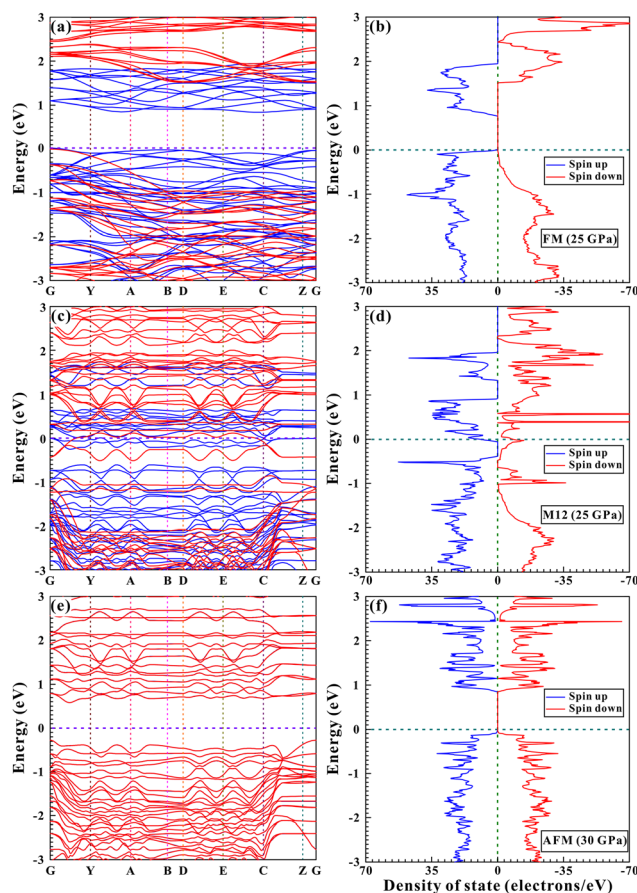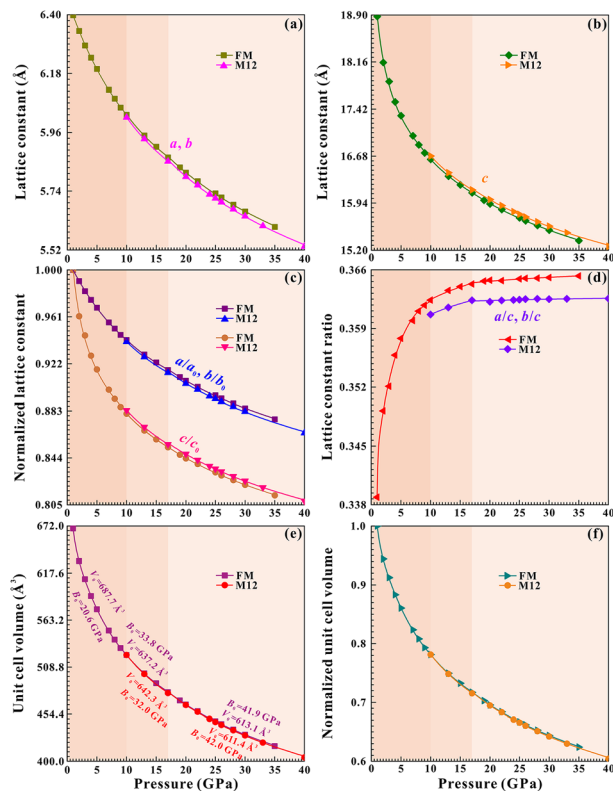
Fig. 11 Theoretical calculation results of (a) and (b) lattice constants (a, b and c); (c) normalized lattice constants (a/a_0, b/b_0 and c/c_0); (d) lattice constant ratios (a/c and b/c); (e) unit cell volume and (f) normalized unit cell volume under pressure within the pressure range of 1–40 GPa. The pressure–volume data of $CrBr_3$ were fitted to the second-order Birch–Murnaghan equation of states to determine its bulk modulus (B_0) and unit cell volume at zero pressure (V_0).
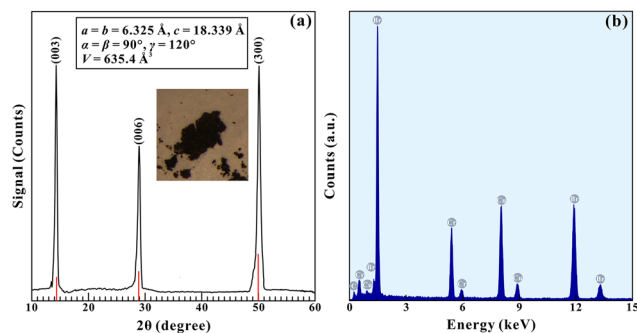

Fig. 12 Structural and compositional characterization of the pristine sample. (a) XRD pattern of the initial sample under ambient conditions. Herein, the red vertical lines represent the standardized peak positions of the rhombohedral $CrBr_3$. Major peaks of the starting sample are marked by (hkl) indices. Inset: an optical micrograph and the corresponding lattice parameters for the starting $CrBr_3$ sample. (b) The EDS result for the pristine sample.

in Fig. 11a–c, the c axis of $CrBr_3$ is more compressible than the a axis owing to the weak van der Waals interlayer bond relative to the strong intralayer covalent bond, which is in accordance with the anisotropic compressibility of 2D layered transition-metal disulfides.[34] Note that the lattice constant ratios (a/c and b/c) of $CrBr_3$ exhibited prominent inflection points at ~10 and ~17 GPa, accompanied by the feeble discontinuity of unit cell volume. Concomitantly, all of these available results including the pressure dependent lattice constants (a, b and c), normalized lattice constants (a/a_0, b/b_0 and c/c_0), Cr–Br–Cr bond angle, nearest Cr–Cr bond length and 2nd nearest Cr–Cr bond length of $CrBr_3$ showed observable inflexion points at ~10 and ~17 GPa. In fact, Ahmad et al. (2020) revealed the emergence of pressure-driven IPT in $CrCl_3$ at 11.0 GPa from the striking inflection point in the lattice constant ratios (a/c and b/c) and a subtle volume discontinuity.[10] As a consequence, the high-pressure structural transitions of $CrBr_3$ at the respective pressures of ~10 and ~17 GPa presumably belong to the second-order phase transformations, as previously reported in other binary compounds of Bi_2S_3, Sb_2S_3, Sb_2Se_3 and VSe_2.[21,39–42] Generally speaking, the transition pressures of $CrBr_3$ obtained from high-pressure experimental and theoretical calculation

results would show a feeble divergence, which is possibly related to the subtle variation of free energy before and after the phase transition.

The calculated pressure–volume relationship of $CrBr_3$ was fitted to three independent second-order Birch–Murnaghan equation of states (BM-EOS) with fixed bulk modulus derivatives of $B'_0 = 4.0$. The fitting results yielded the bulk modulus (B_0) and volume at zero pressure (V_0) to be $B_0 = 20.6$ GPa and $V_0 = 687.7$ Å^3 at 1–10 GPa, $B_0 = 33.8$ GPa and $V_0 = 637.2$ Å^3 at 10–17 GPa as well as $B_0 = 42.0$ GPa and $V_0 = 611.4$ Å^3 at 17–40 GPa. This makes it clear that the high-pressure phases of $CrBr_3$ became incompressible than its low-pressure phase due to the strengthened bond of the sample with the application of pressure.

Conclusion

In the present work, a series of studies on the pressure-driven structural transition, electronic transition and magnetic crossover in the layered chromium tribromide have been firstly reported through Raman spectroscopy, electrical conductivity, HRTEM and first-principles theoretical calculations under different hydrostatic conditions up to 41.3 GPa. Under non-hydrostatic conditions, $CrBr_3$ underwent a second-order phase transformation at 9.5 GPa followed by metallization and FM-to-M12 magnetic transition at 25.9 GPa upon compression; the corresponding reversible phase transformations emerged at 5.0 and 21.7 GPa during the process of decompression. Under hydrostatic conditions, a ~3.0 GPa pressure hysteresis was detectable for the structural and electronic transitions of $CrBr_3$ during both processes of compression and decompression, which is associated with the influence of deviatoric stress. Our present study on $CrBr_3$ sheds light on the interplay between the crystal structure, electronic transition and magnetic switching in the 2D magnetic semiconductor, which is of great

significance for its potential application in spintronic, magnetic and electronic devices.

Experimental

Sample preparation and characterization

High-purity (99.99%) polycrystalline $CrBr_3$ powders with a shiny black colour (inset of Fig. 12a) were commercially purchased from Leshan Kairuida Photoelectric Technology Company, where they were synthesized *via* the chemical vapor deposition method by reacting stoichiometric chromium and bromine powder in a vacuum furnace. We characterized the crystallographic structure of the starting sample by X-ray diffraction (XRD) measurements using an Empyrean-type X-ray powder diffractometer with copper Kα1 radiation. The collected XRD pattern was processed with MDI Jade 6.5 software to determine the lattice parameters of the starting sample. Fig. 12a shows the typical XRD pattern of the starting sample and its corresponding lattice parameters were determined as $a = b = 6.318$ Å, $c = 18.350$ Å, $\alpha = \beta = 90°$, $\gamma = 120°$ and $V = 634.3$ Å^3, which is in good accordance with prior results.[5,43] Concurrently, the quantitative chemical composition analysis on the starting sample was performed using a transmission electron microscope equipped with an energy dispersive X-ray spectroscopy (TEM-EDS) system. As displayed in Fig. 12b, the absence of impurity peaks except the unavoidable carbon and copper peaks from the carbon film proved the high-purity of the starting sample. Furthermore, the atomic ratios of chromium (25.75 at%) : bromine (74.24 at%) elements were determined to be 1 : 2.9, close to the standard chemical formula of $CrBr_3$.

High-pressure Raman spectroscopy experiments

A symmetric piston-cylinder type diamond anvil cell (DAC) having a culet diameter of 200 μm and a bevel angle of 10° was employed for pressure generation and thereby was applied for both high-pressure Raman scattering and electrical conductivity measurements. A sheet of a T-301 stainless steel gasket was pre-pressurized to ~10.0 GPa. Sequentially, a hole of 100 μm diameter was laser-drilled in the middle of indentation as the sample chamber. The starting sample and several fine ruby spheres acting as the pressure calibration were placed into the sample chamber. Two sets of individual high-pressure Raman spectroscopy experiments were performed: one without pressure medium to create non-hydrostatic conditions, and another with helium as the pressure medium to provide hydrostatic conditions, respectively. High-pressure Raman spectra of $CrBr_3$ were recorded using a Renishaw 2000 Micro Confocal Raman spectrometer in a backscattering configuration with a laser wavelength of 514.5 nm emitted from argon ions. The laser power and acquisition time were set to be 1 mW and 5 min for each high-pressure Raman spectrum of $CrBr_3$, respectively. To realize sufficient pressure equilibrium, an appropriate time interval of 15 min was controlled between each Raman scattering measurement. The gathered Raman spectra were precisely fitted by the Lorentzian function to extract the Raman peak positions, Raman FWHMs and spacings in Raman shifts of $CrBr_3$ under pressure.

High-pressure electrical conductivity measurements

In the electrical conductivity experiments of $CrBr_3$, the insulating layer comprising epoxy and boron nitride powder was tightly compressed into the pre-indented stainless-steel gasket having a central hole 180 μm in diameter. Successively, another hole with a diameter of 100 μm was drilled in the middle of indentation, which served as the insulating sample chamber. Furthermore, the remaining section of the gasket was homogeneously coated with insulating cement. Two pieces of platinum electrodes were symmetrically installed to the upper and lower counterparts of the sample chamber and then fastened with silver epoxy. No pressure medium was utilized in electrical conductivity measurements for adequate contact between the sample and electrodes. Complex impedance spectra of $CrBr_3$ were measured with a Solartron-1260 impedance/gain phase analyser in frequency sweeping mode at 10^{-1}–10^7 Hz with a signal voltage of 1.0 V. In variable-temperature electrical conductivity experiments of $CrBr_3$, low temperature conditions were produced by the refrigeration of liquid nitrogen and the temperature was accurately calibrated with a K-type thermocouple attached to the diamond. The details of *in situ* high-pressure Raman scattering and electrical conductivity measurements have been provided in our previous studies.[11,15–20,30,31]

HRTEM observations

Tiny amounts of the starting and recovered samples under different hydrostatic conditions were dispersed onto a copper microgrid coating with holey carbon films for HRTEM and FFT observations, which was performed with a Tecnai G2 F20 S-TWIN TMP system with an accelerating voltage of 200 kV in bright field mode. HRTEM micrographs of samples were recorded with a charge-coupled device digital imaging system. Furthermore, the interplanar spacings of samples were precisely determined using Digital Micrograph software.

Computational details

First-principles theoretical calculations of $CrBr_3$ were carried out within the framework of the density functional theory (DFT) as implemented in the Vienna *ab initio* simulation package (VASP) ranging from 1 to 40 GPa at the Hefei Advanced Computing Center of China. The all-electron projector augmented wave (PAW) method was adopted with $4s^2 4p^5$ and $3d^5 4s^1$ as valence electrons for Br and Cr atoms, respectively. A high plane-wave kinetic cutoff energy of 800 eV was applied to achieve high convergence. The structural relaxation of $CrBr_3$ was conducted until the force on each atom was smaller than 0.01 eV Å^{-1}. Two sufficiently dense k-point meshes of $5 \times 5 \times 3$ and $21 \times 21 \times 7$ are employed to realize the high-quality theoretical calculations of the structural and physical properties in the DFT calculations for a highly symmetric two-dimensional ferromagnetic semiconductor of $CrBr_3$

within the pressure range of 1–40 GPa, which completely satisfied the convergence criteria requirement of the energy difference less than 1 meV per atom. In order to check two coexisting FM and M12 structural phases in $CrBr_3$, the enthalpies of different magnetic configurations including the FM, AFM and M12 phases were calculated within the pressure range of 10–35 GPa under two typical Hubbard U values of 2.0 and 3.2 eV. To accurately determine the pressure point of the structural phase transformation, we also calculated the electronic band structures and density of states of the sample within the pressure range of 25–30 GPa. Furthermore, a series of crystalline parameters including the lattice constants, normalized lattice constants, lattice constant ratios, unit cell volume, normalized unit cell volume, Cr–Br–Cr bond angle, Cr–Br bond length, nearest Cr–Cr bond length and 2nd nearest Cr–Cr bond length with pressure have been successfully obtained within the pressure range of 1–40 GPa. For the FM configuration, all magnetic moments were in the same direction, while the magnetic moments were set to be antiparallel between the nearest neighbours for the AFM configuration. The chromium atom with an opposite electronic spin can result in total magnetic moments up to $12\mu_B$, and thus, it can be nominated as the M12 phase of $CrBr_3$. For more details of the calculation methods and procedures refer to our prior studies.[11,44–46]

Author contributions

Lidong Dai and Haiying Hu performed the conceptualization of this article and led the project. Meiling Hong and Xinyu Zhang performed the investigations including XRD, high-pressure Raman spectroscopy, high-pressure electrical conductivity measurements, and HRTEM analysis. Yu He performed first-principles theoretical calculations. Meiling Hong and Lidong Dai contributed to the analysis, interpretation and discussion of these results. Meiling Hong and Lidong Dai performed the writing – original draft. Meiling Hong, Lidong Dai, Haiying Hu, Xinyu Zhang and Chuang Li performed the writing – review & editing. All the authors commented on the final manuscript. Lidong Dai and Haiying Hu supervised the project.

Conflicts of interest

There are no conflicts to declare.

Acknowledgements

References

1 L. Webster, L. B. Liang and J. A. Yan, Distinct spin-lattice and spin-phonon interactions in monolayer magnetic CrI_3, *Phys. Chem. Chem. Phys.*, 2022, **24**, 17898–17898.

2 B. Nharangatt and R. Chatanathodi, Electronic properties and magnetism of $CrCl_3$ nanoribbons, *J. Magn. Magn. Mater.*, 2022, **564**, 170105.

3 M. A. McGuire, H. Dixit, V. R. Cooper and B. C. Sales, Coupling of crystal structure and magnetism in the layered, ferromagnetic insulator CrI_3, *Chem. Mater.*, 2015, **27**, 4165–4165.

4 X. Y. Yu, X. Zhang, Q. Shi, S. J. Tian, H. C. Lei, K. Xu and H. Hosono, Large magnetocaloric effect in van der Waals crystal $CrBr_3$, *Front. Phys.*, 2019, **14**, 43501.

5 D. P. Kozlenko, O. N. Lis, S. E. Kichanov, E. V. Lukin, N. M. Belozerova and B. N. Savenko, Spin-induced negative thermal expansion and spin-phonon coupling in van der Waals material $CrBr_3$, *npj Quantum Mater.*, 2021, **6**, 19.

6 B. Huang, G. Clark, E. Navarro-Moratalla, D. R. Klein, R. Cheng, K. L. Seyler, D. Zhong, E. Schmidgall, M. A. McGuire, D. H. Cobden, W. Yao, D. Xiao, P. Jarillo-Herrero and X. D. Xu, Layer-dependent ferromagnetism in a van der Waals crystal down to the monolayer limit, *Nature*, 2017, **546**, 270–273.

7 W. C. Jin, H. H. Kim, Z. P. Ye, S. W. Li, P. Rezaie, F. B. Diaz, S. Siddiq, E. Wauer, B. W. Yang, C. H. Li, S. J. Tian, K. Sun, H. C. Lei, A. W. Tsen, L. Y. Zhao and R. He, Raman fingerprint of two terahertz spin wave branches in a two-dimensional honeycomb Ising ferromagnet, *Nat. Commun.*, 2018, **9**, 5122.

8 L. Webster and J. A. Yan, Strain-tunable magnetic anisotropy in monolayer $CrCl_3$, $CrBr_3$, and CrI_3, *Phys. Rev. B*, 2018, **98**, 144411.

9 I. Pollini, Electronic structure of $CrBr_3$ studied by X-ray photoelectron spectroscopy, *Phys. Rev. B: Condens. Matter Mater. Phys.*, 1999, **60**, 16170–16175.

10 A. S. Ahmad, Y. C. Liang, M. D. Dong, X. F. Zhou, L. M. Fang, Y. H. Xia, J. H. Dai, X. Z. Yan, X. H. Yu, J. F. Dai, G. J. Zhang, W. Q. Zhang, Y. S. Zhao and S. M. Wang, Pressure-driven switching of magnetism in layered $CrCl_3$, *Nanoscale*, 2020, **12**, 22935–22944.

11 M. L. Hong, L. D. Dai, H. Y. Hu, X. Y. Zhang, C. Li and Y. He, Pressure-induced structural phase transition and metallization of $CrCl_3$ under different hydrostatic environments up to 50.0 GPa, *Inorg. Chem.*, 2022, **61**, 4852–4864.

12 A. Ghosh, D. Singh, T. Aramaki, Q. G. Mu, V. Borisov, Y. Kvashnin, G. Haider, M. Jonak, D. Chareev, S. A. Medvedev, R. Klingeler, M. Mito, E. H. Abdul-Hafidh, J. Vejpravova, M. Kalbàč, R. Ahuja, O. Eriksson and M. Abdel-Hafiez, Exotic magnetic and electronic properties of layered CrI_3 single crystals under high pressure, *Phys. Rev. B*, 2022, **105**, L081104.

13 O. Lis, D. Kozlenko, S. Kichanov, E. Lukin, I. Zel and B. Savenko, Structural, magnetic and vibrational properties of van der Waals ferromagnet $CrBr_3$ at high pressure, *Materials*, 2023, **16**, 454.

14 S. Duwal and C. S. Yoo, Shear-induced isostructural phase transition and metallization of layered tungsten disulfide under nonhydrostatic compression, *J. Phys. Chem. C*, 2016, **120**, 5101–5107.

15 Y. K. Zhuang, L. D. Dai, L. Wu, H. P. Li, H. Y. Hu, K. X. Liu, L. F. Yang and C. Pu, Pressure-induced permanent metallization with reversible structural transition in molybdenum disulfide, *Appl. Phys. Lett.*, 2017, **110**, 122103.

16 Y. K. Zhuang, L. D. Dai, H. P. Li, H. Y. Hu, K. X. Liu, L. F. Yang, C. Pu, M. L. Hong and P. F. Liu, Deviatoric stresses promoted metallization in rhenium disulfide, *J. Phys. D: Appl. Phys.*, 2018, **51**, 165101.

17 L. F. Yang, L. D. Dai, H. P. Li, H. Y. Hu, K. X. Liu, C. Pu, M. L. Hong and P. F. Liu, Pressure-induced metallization in $MoSe_2$ under different pressure conditions, *RSC Adv.*, 2019, **9**, 5794–5803.

18 L. F. Yang, L. D. Dai, H. P. Li, H. Y. Hu, K. X. Liu, C. Pu, M. L. Hong and P. F. Liu, Characterization of the pressure-induced phase transition of metallization for $MoTe_2$ under hydrostatic and non-hydrostatic conditions, *AIP Adv.*, 2019, **9**, 065104.

19 X. Y. Zhang, L. D. Dai, H. Y. Hu, M. L. Hong and C. Li, Pressure-induced coupled structural-electronic transition in SnS_2 under different hydrostatic environments up to 39.7 GPa, *RSC Adv.*, 2022, **12**, 2454–2461.

20 M. L. Hong, L. D. Dai, H. Y. Hu, X. Y. Zhang, C. Li and Y. He, High-pressure structural phase transitions and metallization in layered HfS_2 under different hydrostatic environments up to 42.1 GPa, *J. Mater. Chem. C*, 2022, **10**, 10541–10550.

21 I. Efthimiopoulos, J. M. Zhang, M. Kucway, C. Y. Park, R. C. Ewing and Y. J. Wang, Sb_2Se_3 under high pressure, *Sci. Rep.*, 2013, **3**, 2665.

22 V. M. Bermudez, Unit-cell vibrational spectra of chromium trichloride and chromium tribromide, *Solid State Commun.*, 1976, **19**, 693–697.

23 T. T. Yin, K. A. Ulman, S. Liu, A. G. del Águila, Y. Q. Huang, L. F. Zhang, M. Serra, D. Sedmidubsky, Z. Sofer, S. Y. Quek and Q. H. Xiong, Chiral phonons and giant magneto-optical effect in $CrBr_3$ 2D magnet, *Adv. Mater.*, 2021, **33**, 2101618.

24 Y. J. Zhang, G. M. Li, S. H. Pei, B. B. Lyu, Q. L. Huang, X. W. Wang, W. He and M. Y. Huang, Self-modulated photoluminescence of $CrBr_3$ flake, *Micro Nano Lett.*, 2020, **15**, 788–792.

25 L. D. Dai, C. Pu, H. P. Li, H. Y. Hu, K. X. Liu, L. F. Yang and M. L. Hong, Characterization of metallization and amorphization for GaP under different hydrostatic environments in diamond anvil cell up to 40.0 GPa, *Rev. Sci. Instrum.*, 2019, **90**, 066103.

26 K. Ahadi, L. Galletti, Y. T. Li, S. Salmani-Rezaie, W. Z. Wu and S. Stemmer, Enhancing superconductivity in $SrTiO_3$ films with strain, *Sci. Adv.*, 2019, **5**, eaaw0120.

27 C. Liu, X. Q. Song, Q. Li, Y. M. Ma and C. F. Chen, Smooth flow in diamond: Atomistic ductility and electronic conductivity, *Phys. Rev. Lett.*, 2019, **123**, 195504.

28 C. Liu, X. Q. Song, Q. Li, Y. M. Ma and C. F. Chen, Superconductivity in compression-shear deformed diamond, *Phys. Rev. Lett.*, 2020, **124**, 147001.

29 X. Q. Song, C. Liu, Q. Li, R. J. Hemley, Y. M. Ma and C. F. Chen, Stress-induced high-T_c superconductivity in solid molecular hydrogen, *Proc. Natl. Acad. Sci. U. S. A.*, 2022, **26**, e2122691119.

30 L. F. Yang, J. J. Jiang, L. D. Dai, H. Y. Hu, M. L. Hong, X. Y. Zhang, H. P. Li and P. F. Liu, High-pressure structural phase transition and metallization in Ga_2S_3 under non-hydrostatic and hydrostatic conditions up to 36.4 GPa, *J. Mater. Chem. C*, 2021, **9**, 2912–2918.

31 L. D. Dai, K. X. Liu, H. P. Li, L. Wu, H. Y. Hu, Y. K. Zhuang, L. F. Yang, C. Pu and P. F. Liu, Pressure-induced irreversible metallization accompanying the phase transitions in Sb_2S_3, *Phys. Rev. B*, 2018, **97**, 024103.

32 W. Z. Cai, L. Yan, S. K. Chong, J. G. Xu, D. Z. Zhang, V. V. Deshpande, L. J. Zhou and S. Deemyad, Pressure-induced metallization in the absence of a structural transition in the layered ferromagnetic insulator $Cr_2Ge_2Te_6$, *Phys. Rev. B*, 2022, **106**, 085116.

33 H. Wang, V. Eyert and U. Schwingenschlögl, Electronic structure and magnetic ordering of the semiconducting chromium trihalides $CrCl_3$, $CrBr_3$, and CrI_3, *J. Phys.: Condens. Matter*, 2011, **23**, 116003.

34 X. M. Zhao, H. Y. Liu, A. F. Goncharov, Z. W. Zhao, V. V. Struzhkin, H. K. Mao, A. G. Gavriliuk and X. J. Chen, Pressure effect on the electronic, structural, and vibrational properties of layered $2H$-$MoTe_2$, *Phys. Rev. B*, 2019, **99**, 024111.

35 Z. Zhao, H. J. Zhang, H. T. Yuan, S. B. Wang, Y. Lin, Q. S. Zeng, G. Xu, Z. X. Liu, G. K. Solanki, K. D. Patel, Y. Cui, H. Y. Hwang and W. L. Mao, Pressure induced metallization with absence of structural transition in layered molybdenum diselenide, *Nat. Commun.*, 2015, **6**, 7312.

36 C. Tian, Y. P. Gao, F. B. Tian, X. Wang, Z. H. Zhang, D. F. Duan, X. L. Huang and T. Cui, Dimensionality switching and superconductivity transition in dense $1T$-$HfSe_2$, *Phys. Rev. B*, 2022, **105**, L180506.

37 P. G. Naumov, M. A. Eighazali, H. Mirhosseini, V. Süβ, E. Morosan, C. Felser and S. A. Medvedev, Pressure-induced metallization in layered $ReSe_2$, *J. Phys.: Condens. Matter*, 2018, **30**, 035401.

38 W. Lei, W. Wang, X. Ming, S. L. Zhang, G. Tang, X. J. Zheng, H. Li and C. Autieri, Structural transition,

metallization, and superconductivity in quasi-two-dimensional layered PdS_2 under compression, *Phys. Rev. B*, 2020, **101**, 205149.

39 C. Y. Li, J. G. Zhao, Q. Y. Hu, Z. G. Liu, Z. H. Yu and H. Yan, Crystal structure and transporting properties of Bi_2S_3 under high pressure: Experimental and theoretical studies, *J. Alloys Compd.*, 2016, **688**, 329–335.

40 I. Efthimiopoulos, J. Kemichick, X. Zhou, S. V. Khare, D. Ikuta and Y. J. Wang, High-pressure studies of Bi_2S_3, *J. Phys. Chem. A*, 2014, **118**, 1713–1720.

41 I. Efthimiopoulos, C. Buchan and Y. J. Wang, Structural properties of Sb_2S_3 under pressure: evidence of an electronic topological transition, *Sci. Rep.*, 2016, **6**, 24246.

42 S. Pal, K. Debnath, S. N. Gupta, L. Harnagea, D. V. S. Muthu, U. V. Waghmare and A. K. Sood, Pressure-induced $1T$ to $3R$ structural phase transition in metallic VSe_2: X-ray diffraction and first-principles theory, *Phys. Rev. B*, 2021, **104**, 014108.

43 W. B. Zhang, Q. Qu, P. Zhu and C. H. Lam, Robust intrinsic ferromagnetism and half semiconductivity in stable two-dimensional single-layer chromium trihalides, *J. Mater. Chem. C*, 2015, **3**, 12457.

44 Y. He, S. C. Sun, D. Y. Kim, B. G. Jang, H. P. Li and H.-K. Mao, Superionic iron alloys and their seismic velocities in Earth's inner core, *Nature*, 2022, **602**, 258.

45 S. C. Sun, Y. He, J. Y. Yang, Y. F. Lin, J. F. Li, D. Y. Kim, H. P. Li and H.-K. Mao, Superionic effect and anisotropic texture in Earth's inner core driven by geomagnetic field, *Nat. Commun.*, 2023, **14**, 1656.

46 Y. He, L. D. Dai, D. Y. Kim, H. P. Li and S. Karato, Thermal ionization of hydrogen in hydrous olivine with enhanced and anisotropic conductivity, *J. Geophys. Res.: Solid Earth*, 2021, **126**, e2021JB022939.